JOURNAL OF APPLIED PHYSICS **113**, 183707 (2013)

Calculated thermoelectric properties of $In_xGa_{1-x}N$, $In_xAl_{1-x}N$, and $Al_xGa_{1-x}N$

Alexander Sztein,[1,a)] John Haberstroh,[2] John E. Bowers,[1,3] Steven P. DenBaars,[1,3] and Shuji Nakamura[1,3]
[1]*Materials Department, University of California, Santa Barbara, California 93106, USA*
[2]*Physics Department, University of California, Santa Barbara, California 93106, USA*
[3]*Electrical and Computer Engineering Department, University of California, Santa Barbara, California 93106, USA*

(Received 9 April 2013; accepted 22 April 2013; published online 10 May 2013)

The thermoelectric properties of III-nitride materials are of interest due to their potential use for high temperature power generation applications and the increasing commercial importance of the material system; however, the very large parameter space of different alloy compositions, carrier densities, and range of operating temperatures makes a complete experimental exploration of this material system difficult. In order to predict thermoelectric performances and identify the most promising compositions and carrier densities, the thermoelectric properties of $In_xGa_{1-x}N$, $In_xAl_{1-x}N$, and $Al_xGa_{1-x}N$ are modeled. The Boltzmann transport equation is used to calculate the Seebeck coefficient, electrical conductivity, and the electron component of thermal conductivity. Scattering mechanisms considered for electronic properties include ionized impurity, alloy potential, polar optical phonon, deformation potential, piezoelectric, and charged dislocation scattering. The Callaway model is used to calculate the phonon component of thermal conductivity with Normal, Umklapp, mass defect, and dislocation scattering mechanisms included. Thermal and electrical results are combined to calculate ZT values. $In_xGa_{1-x}N$ is identified as the most promising of the three ternary alloys investigated, with a calculated ZT of 0.85 at 1200 K for $In_{0.1}Ga_{0.9}N$ at an optimized carrier density. $Al_xGa_{1-x}N$ is predicted to have a ZT of 0.57 at 1200 K under optimized composition and carrier density. $In_xAl_{1-x}N$ is predicted to have a ZT of 0.33 at 1200 K at optimized composition and carrier density. Calculated Seebeck coefficients, electrical conductivities, thermal conductivities, and ZTs are compared with experimental data where such data are available. © *2013 AIP Publishing LLC*. [http://dx.doi.org/10.1063/1.4804174]

I. INTRODUCTION

Gallium nitride based materials are increasingly used in a wide variety of applications including light emitting diodes, laser diodes, power amplifiers, and solar cells, with a wide variety of commercial products already available.[1,2] In addition to these applications, their potential suitability as a high temperature thermoelectric material has been suggested by a number of authors.[3–5]

Thermoelectrics are capable of converting heat into electricity and have recently received significant attention for waste heat recovery applications.[6,7] The major limiting factors in their commercial deployment are high cost and relatively low efficiency. In order to improve efficiencies, new materials with higher thermoelectric figures of merit, ZT, must be developed. ZT is directly related to the maximum theoretical efficiency of a thermoelectric device and is given by

$$ZT = \frac{S^2\sigma}{\kappa_{lattice} + \kappa_{electron}}T, \quad (1)$$

where S is the Seebeck coefficient, σ is the electrical conductivity, κ is the thermal conductivity due to both the lattice and electron conduction, and T is the temperature.

The importance of improving ZT, the need for higher temperature thermoelectrics for waste heat recovery, and the need for non-toxic thermoelectrics make it necessary to explore a wide range of potential materials. The family of III-nitrides, including GaN, InN, AlN, and their alloys has both the requisite large band gaps and thermal stabilities to operate at elevated temperatures and are thus an important prospective high temperature thermoelectric material system. Additionally, GaN is non-toxic, an important consideration for distributed applications such as automobile waste heat recovery.[8]

The potential of III-nitride materials for thermoelectric applications has motivated increasing research on the experimental properties of GaN,[9,10] InGaN,[3,5,11,12] InAlN,[13–15] and AlInGaN[16,17] as well as III-nitride based thermoelectric devices.[18] There have also been a few attempts to calculate and predict the properties of these materials, most notably the thermoelectric properties of GaN,[4] AlGaN,[4,19] and InGaN.[19,20] These studies all use the Boltzmann transport equation (BTE) with the relaxation time approximation (RTA) to calculate the electrical transport properties and the Callaway model along with the virtual crystal approximation for phonon transport. There is some limited agreement in these works between calculated thermal conductivity and experimentally reported values; however, the electrical properties show significant deviation from reported experimental values. In particular, electrical conductivity is overestimated and Seebeck coefficient is underestimated. This problem

a)E-mail: asztein@umail.ucsb.edu

 © 2013 AIP Publishing LLC

becomes more acute as carrier concentration increases. More accurate modeling of thermoelectric properties in the III-nitride system would allow a rapid optimization of thermoelectric properties over a wide parameter space. In addition, modeling can predict the properties of materials that for practical reasons are currently extremely difficult to fabricate and measure experimentally.

The current work significantly improves upon the previous work and calculates electrical conductivities, Seebeck coefficients, and thermal conductivities with greatly improved accuracy. In addition, the calculations are extended to include InAlN. The validity of the current model is demonstrated through comparison of each individual calculated parameter with experimental data where available. Some of the added considerations as compared to previous works include the treatment of both degenerate and non-degenerate carrier concentrations for ionized impurity scattering, the consideration of non-parabolic bands, and the inclusion of the alloy scattering mechanism for electrical properties.

II. ELECTRON TRANSPORT MODEL

Using the BTE and the assumption that local deviations from equilibrium are small, one can determine expressions for a material's electrical conductivity, Seebeck coefficient, and electron component of thermal conductivity. The derivation of these properties from the BTE is not shown here as they are available from Refs. 7, 21, and 22. The use of the BTE and relaxation time approximation for thermoelectric calculations has been validated by extensive agreement between calculations and experimental results in material systems including InGaAlAs, SiGe, and PbTe.[21,23,24] The electrical conductivity, σ, Seebeck coefficient, S, and electron thermal conductivity, κ_e, are given by

$$\sigma = \int \sigma_d(E)dE, \tag{2}$$

$$S = \frac{1}{eT}\left(\frac{\int \sigma_d(E)(E-E_F)dE}{\int \sigma_d(E)dE}\right), \tag{3}$$

$$\kappa_e = \frac{1}{e^2T}\left(\int \sigma_d(E)(E-E_F)^2dE - \frac{\left(\int \sigma_d(E)(E-E_F)dE\right)^2}{\int \sigma_d(E)dE}\right), \tag{4}$$

where e is the elementary charge, E is the electron energy, E_F is the Fermi level referenced to the conduction band minima, and σ_d is the differential conductivity

$$\sigma_d(E) = e^2\tau(E)\upsilon^2(E)\rho_{DOS}(E)\left(-\frac{\partial f_0}{\partial E}\right). \tag{5}$$

The differential conductivity defines the contribution of electrons at energy level E to the electrical conductivity. $\tau(E)$, $\upsilon(E)$, $\rho_{DOS}(E)$, and $f_0(E)$ are, respectively, the energy dependent scattering rate, electron velocity, electron density of states, and Fermi-Dirac distribution. This work only considers electrons in the conduction band as most III-nitride materials are n-type and band gaps are wide enough that there is no significant thermal excitation and thus no significant concentration of holes. In a very small subset of experimental conditions near InN at high temperatures, this assumption is no longer valid and will be specifically pointed out when applicable.

In this work, the electron energy is defined using the Kane model and takes into account band non-parabolicity through the dispersion ratio[21,22]

$$\gamma(\mathrm{E}) = E(1+\alpha E) = \frac{\hbar^2k^2}{2m^*}, \tag{6}$$

where α is the non-parabolicity parameter, $\hbar$ is Planck's constant, k is the electron wave vector, and m^* is the effective mass. Band non-parabolicity is important to take into account when the carrier density is high and the bands can be filled to higher energies where the parabolic band model is no longer valid. These effects are stronger for materials with smaller band gaps, which tend to yield larger non-parabolicity parameters.

Use of the Kane model leads to the following definitions for density of states and electron velocity[21,22]

$$\rho_{DOS}(E) = \frac{2^{1/2}(m^*)^{3/2}}{\pi^2\hbar^3}(E+\alpha E^2)^{1/2}(1+2\alpha E), \tag{7}$$

$$\upsilon^2(E) = \frac{2}{3m^*}\frac{E(1+\alpha E)}{(1+2\alpha E)^2}. \tag{8}$$

The Fermi level is determined numerically from the expression for carrier density

$$n = \int_0^\infty \rho_{DOS}(E)f_0(E)dE, \tag{9}$$

which accurately takes into account non-parabolic bands and both degenerate and non-degenerate carrier statistics. The carrier concentration is assumed to be equal to the number of dopant atoms, since silicon, the most common n-type dopant for this material system, has been shown to be a shallow donor with an ionization ratio near unity at 300 K.[25]

The energy dependent electron relaxation time is defined using the RTA[4]

$$\tau^{-1}(E) = \sum \tau_i^{-1}(E), \tag{10}$$

where each index, i, represents an individual scattering term. In this work, the scattering mechanisms considered are ionized impurity scattering, alloy scattering, polar optical phonon scattering, piezoelectric scattering, deformation potential scattering, and charged dislocation scattering. These terms are shown in previous work to represent the dominant scattering mechanisms in III-nitride materials.[4,26–29] It is important to note that the RTA is valid only for elastic and isotropic scattering. In particular, of the scattering mechanisms used in this work, polar optical phonon scattering violates this assumption.

If this mechanism becomes the dominant scattering mechanism, then this approximation is no longer valid and either an iterative approach[30] or a full Monte Carlo approach[28,29] must be used. This is fortunately not the case in this work as thermoelectric materials tend to be highly doped and are often ternary or quaternary alloys, making ionized impurity and alloy scattering the dominant scattering mechanisms.

The relaxation time for ionized impurity scattering in terms of the dispersion ratio $\gamma(E)$ and density of states $\rho_{DOS}(E)$ is given by[31]

$$\tau_{II}^{-1} = \frac{\pi Z^2 e^4 N_{II} \hbar^3}{32\varepsilon_s^2 m^{*2}\gamma^2(E)}\rho_{DOS}(E)\left[\log\left(\frac{8m^*\gamma(E)L_D^2}{\hbar^2}+1\right) - \frac{1}{1+\hbar^2/8m^*L_D^2\gamma(E)}\right], \tag{11}$$

where N_{II} is the number of ionized impurities, ε_s is the static dielectric constant, Z is the ionization number (unity for silicon donors), and L_D is the screening length. Since thermoelectric materials often have high carrier concentrations and can be either degenerate or non-degenerate, it is important to use the exact screening length as given by Fermi-Dirac statistics

$$L_D = \frac{1}{e}\sqrt{\frac{\varepsilon_s}{\partial n/\partial E_F}}, \tag{12}$$

$$\frac{\partial n}{\partial E_F} = \int_0^\infty \rho_{DOS}(E)\left(\frac{df_0}{dE_F}\right)dE. \tag{13}$$

The next scattering mechanism considered is alloy scattering. This is a very important scattering mechanism for ternary III-nitride materials and is given by[1,21,32]

$$\tau_{Alloy}^{-1} = \frac{3\pi}{8\sqrt{2}}\frac{(m^*)^{3/2}}{\hbar^4}\Omega x(1-x)(\Delta U)^2[\gamma(E)]^{1/2}\frac{d\gamma(E)}{dE}s, \tag{14}$$

where Ω is the primitive cell volume, x is the alloy composition, ΔU is the alloy scattering potential, and s is a parameter which describes the effect of ordering in the alloy. For this work, the alloy elements are assumed to be randomly distributed and s is set to one. There are a variety of different methods used to calculate the alloy scattering potential based on conduction band offsets,[1,28,33] electron affinity differences,[1,21,33] or electronegativity theory,[1,28,33,34] but there is very little agreement across different works and material systems and thus alloy scattering potential is typically used as fitting parameter to experimental data. In this work, the alloy scattering potential is obtained by fitting to experimental data when literature values are not available.

Polar optical phonon scattering is given by[4,35]

$$\tau_{POP}^{-1} = \frac{e^2}{4\pi\hbar}\left(\frac{2m^*\omega}{\hbar}\right)^{1/2}\left(\frac{1}{\varepsilon_\infty}-\frac{1}{\varepsilon_s}\right)[n(\omega)+1]\frac{f_0(E+\hbar\omega)}{f_0(E)}\left(\frac{\hbar\omega}{E}\right)^{1/2}\sinh^{-1}\left(\frac{E}{\hbar\omega}\right)^{1/2}, \tag{15}$$

where ω is the optical phonon frequency, $n(\omega)$ is the phonon occupation as given by Bose-Einstein statistics, and ε_∞ is the high frequency dielectric constant.

Piezoelectric scattering is given by[31]

$$\tau_{pe}^{-1} = \frac{\pi e^2 K_{av}^2 \hbar k_b T}{4\varepsilon_s m^*}\frac{\rho_{DOS}(E)}{\gamma(E)}I^2(\mathbf{k}',\mathbf{k})H(E), \tag{16}$$

where

$$H(E) = 1 - \frac{\hbar^2}{4m^*L_D^2\gamma(E)}\log\left(\frac{8m^*L_D^2\gamma(E)}{\hbar^2}+1\right) + \frac{1}{8m^*L_D^2\gamma(E)\hbar^{-2}+1} \tag{17}$$

and K_{av}^2 is the average electromechanical coupling coefficient as calculated according to Ridley *et al.*[35] and $I^2(\mathbf{k}',\mathbf{k})$ is a factor which represents the wave function overlap integral over the unit cell before and after scattering, which is taken to be unity.[31]

Deformation potential scattering, sometimes known as acoustic phonon scattering, is given by[31]

$$\tau_{def}^{-1} = \pi\frac{D_{ac}^2 k_b T}{\hbar c_L}I^2(\mathbf{k}',\mathbf{k})\rho_{DOS}(E), \tag{18}$$

where D_{ac} is the deformation potential and c_L is the average elastic constant for longitudinal modes which can be calculated from the elastic stiffness coefficients $c_{i,j}$

$$c_L = c_{11} + \frac{2}{5}(c_{12}+2c_{44}-c_{11}). \tag{19}$$

The last scattering mechanism is charged dislocation scattering, where the relaxation time is given by[4,36]

$$\tau_{dis}^{-1} = \frac{N_{dis}m^*e^4}{\hbar^3\varepsilon_s^2 c^2}\frac{L_D^4}{(1+4L_D^2k_\perp^2)^{3/2}}, \tag{20}$$

where c is the lattice constant along the $\langle 0001\rangle$ direction, N_{dis} is the number of dislocation lines perpendicular to the (0001) plane, and $k_\perp$ is the component of the wave vector perpendicular to the dislocation direction. Crystallographic directions are chosen assuming c-plane growth and in-plane thermoelectric measurements to match available experimental data. For all calculations in this work, the dislocation density is set to $1\times10^9\,\mathrm{cm}^{-2}$, which is high, but a typical dislocation density for GaN on sapphire.[37]

III. PHONON TRANSPORT MODEL

The lattice component of thermal conductivity is calculated following the model first proposed by Callaway,[38] with the virtual crystal extension later developed by Abeles.[39] The virtual crystal model accounts for the alloying of two separate constituent materials, which in this case are two binary alloys that combine to create a ternary alloy. These models have been extensively used and verified through

comparison to experiment for a variety of material systems including both group IV and alloyed III-V materials.[40–42]

Following these works, the lattice thermal conductivity of a material can be represented by[40]

$$\kappa_{lattice} = \kappa_1 + \kappa_2, \tag{21}$$

$$\kappa_1 = \frac{k_b^4 T^3}{2\hbar^3 \pi^2 \upsilon} \int_0^{\theta/T} \tau_C(x) \frac{x^4 e^x}{(e^x - 1)^2} dx, \tag{22}$$

$$\kappa_2 = \frac{k_b^4 T^3}{2\hbar^3 \pi^2 \upsilon} \frac{\left[\int_0^{\theta/T} \frac{\tau_C(x)}{\tau_N(x)} \frac{x^4 e^x}{(e^x - 1)^2} dx\right]^2}{\int_0^{\theta/T} \frac{\tau_C(x)}{\tau_N(x)\tau_R(x)} \frac{x^4 e^x}{(e^x - 1)^2} dx}, \tag{23}$$

where υ is the averaged sound velocity as calculated in Liu *et al.*,[42] θ is the Debye temperature, τ_N is the phonon scattering time due normal scattering, τ_R is the combined scattering time due to all resistive processes, and τ_C is the combined phonon relaxation time due to both normal and resistive processes. Whether a scattering mechanism is normal or resistive will be indicated below. The relaxation time approximation is once again used to combine relaxation times as described in Eq. (10). The variable of integration x is related to the phonon frequency, ω, and is defined by

$$x = \frac{\hbar\omega}{k_b T}. \tag{24}$$

The virtual crystal model is used to apply the Callaway model to random alloys. The virtual crystal model replaces the random alloy with an ordered virtual crystal whose attributes are a mixture of the constituent materials. Deviations from this virtual crystal then cause scattering of phonons.[32,42] The virtual atomic weight, M, is the average of the alloy components

$$M = x_A M_A + (1 - x_A) M_B, \tag{25}$$

where x_A is the mass fraction of alloy constituent A, and M_A and M_B are the atomic masses of constituents A and B, respectively. In this work, A and B represent GaN, InN, and AlN depending on which ternary material is being modeled. The virtual atomic volume is assumed to follow Vegard's Law and is given by

$$\delta = x_A \delta_A + (1 - x_A)\delta_B, \tag{26}$$

where δ is the cube root of the virtual atomic volume.

The scattering times are split into normal scattering and resistive scattering processes. The normal scattering term describes phonon-phonon scattering events where momentum is conserved and is given by[41]

$$\tau_N^{-1}(x) = \frac{k_b^3 \gamma^2 V}{M\hbar^2 \upsilon^5} \left(\frac{k_b}{\hbar}\right)^2 x^2 T^5, \tag{27}$$

where γ is the Grüneisen parameter, V is the volume per atom, and M is the virtual atomic mass. Since phonon momentum is conserved in normal scattering, it does not directly limit thermal conductivity, but it does affect the phonon distribution in momentum and energy space. This modification of phonon distribution has an indirect impact on thermal conductivity and must be included.[41] The resistive processes do not conserve phonon momentum and thus contribute directly to thermal conductivity. The resistive processes considered in this work are Umklapp scattering, mass defect scattering, boundary scattering, and dislocation scattering. Umklapp scattering describes phonon-phonon scattering events where momentum is not conserved and is given by[41]

$$\tau_U^{-1}(x) = B_U \left(\frac{k_b}{\hbar}\right)^2 x^2 T^3 \exp[-\theta/3T], \tag{28}$$

where B_U is given by

$$B_U = \frac{\hbar\gamma^2}{M\upsilon^2\theta}. \tag{29}$$

Mass defect scattering is a very important scattering term in these heavily doped and alloyed systems and describes the scattering of phonons due to impurity atoms in the lattice. The treatment of mass defect scattering, also known as point defect scattering, follows the approach of Liu *et al.*[42]

$$\tau_M^{-1} = \frac{\delta^3 \Gamma \omega^4}{4\pi\upsilon^3}, \tag{30}$$

where

$$\Gamma = \sum_i x_i \left(\left[\frac{M_i - M}{M}\right]^2 + \varepsilon\left[\frac{\delta_i - \delta}{\delta}\right]^2\right) \tag{31}$$

and i represents each type of atomic mass defect from the virtual crystal. x_i is the atomic fraction of sites occupied by

TABLE I. Material parameters used in the calculation of thermoelectric properties.

Parameter[a]	GaN	InN	AlN
Static dielectric constant, ε_s	9.5 ε_0	15.3 ε_0	9.14 ε_0
High frequency dielectric constant, ε_∞	5.35 ε_0	8.4 ε_0	4.6 ε_0
Effective mass, m^*	0.27 m_0	0.115 m_0	0.35 m_0
Nonparabolicity parameter, α (eV^{-1})	0.189[b]	1.43[b]	0.044[b]
Optical phonon energy, $\hbar\omega_{LO}$ (meV)	91.2	89.0	99.2
Debye temperature, Θ (K)	600	660	1150
Grüneisen parameter, γ	0.5[c]	0.3[d]	0.5[e]
a (Å)	3.16	3.54	3.11
c (Å)	5.17	5.76	4.98
Ionic radius group III, R_i (Å)	0.93	1.06	0.85
C_{11} (GPa)	390	223	410
C_{12} (GPa)	145	115	149
C_{44} (GPa)	105	48	125
Deformation potential, D_{ac} (eV)	8.3	7.1	9.5

[a]Unless otherwise noted all parameters are taken from Ref. 1.
[b]Ref. 29.
[c]Ref. 4.
[d]Fitted to experimental data.
[e]Ref. 47.

TABLE II. Alloy scattering potentials used in the calculation of alloy scattering times.

Parameter	InGaN	AlGaN	InAlN
Alloy scattering potential, U_{AB} (eV)	1.2[a]	1.8[b]	2.8[a]

[a]No literature value available, used as fitting parameter to experiment within range provided in Ref. 1.
[b]Ref. 48.

defect i, M_i is the atomic mass of element i, δ_i is the atomic radius of element i, and ε is a parameter which accounts for the strain present in the lattice due to atomic radius differences. The value of ε is set equal to 39 following the assumptions made by Liu *et al.*[42] For this work, each of the two group III elements present in the ternary alloy along with the silicon dopant atoms are considered.

Separate scattering times are calculated for scattering due to dislocation cores and the elastic fields due to screw, edge, and mixed dislocations

$$\tau_{Dis}^{-1} = \tau_{Core}^{-1} + \tau_{Edge}^{-1} + \tau_{Screw}^{-1} + \tau_{Mixed}^{-1}. \quad (32)$$

The specific details of the treatment for each of these dislocation types in the gallium nitride system are described in detail by Zou *et al.*[37]

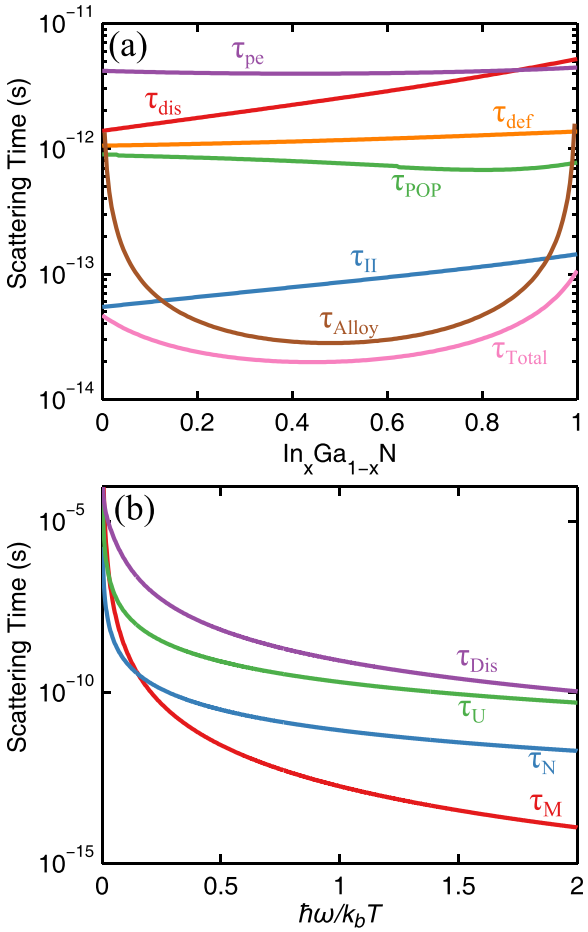

FIG. 1. (a) Electron scattering times versus composition for $In_xGa_{1-x}N$ at 300 K and 1×10^{19} cm^{-3} carrier concentration. (b) Phonon scattering times versus $\hbar\omega/k_bT$ at $In_{0.1}Ga_{0.9}N$, 300 K and 1×10^{19} cm^{-3} carrier concentration.

The material parameters and constants used in this work are given in Tables I and II. For alloy compositions, all values were extrapolated linearly between the two binary materials,[1,20] except where specific composition dependence relationships are available, as is the case for Debye temperature[39] and the elastic constants.[39]

IV. RESULTS AND DISCUSSION

A. InGaN

Figure 1(a) shows example electron scattering times versus composition as calculated for $In_xGa_{1-x}N$ at 300 K with a carrier density of 1×10^{19} cm^{-3}. Scattering times such as these form the core of the electrical modeling in this work and are used to calculate the transport parameters as defined in Eqs. (2)–(4). It can be seen from Figure 1(a) that either ionized impurity or alloy scattering is dominant depending on indium composition. This is true for all alloys and experimental conditions presented in this work, with ionized impurity scattering dominant near the binary compositions and

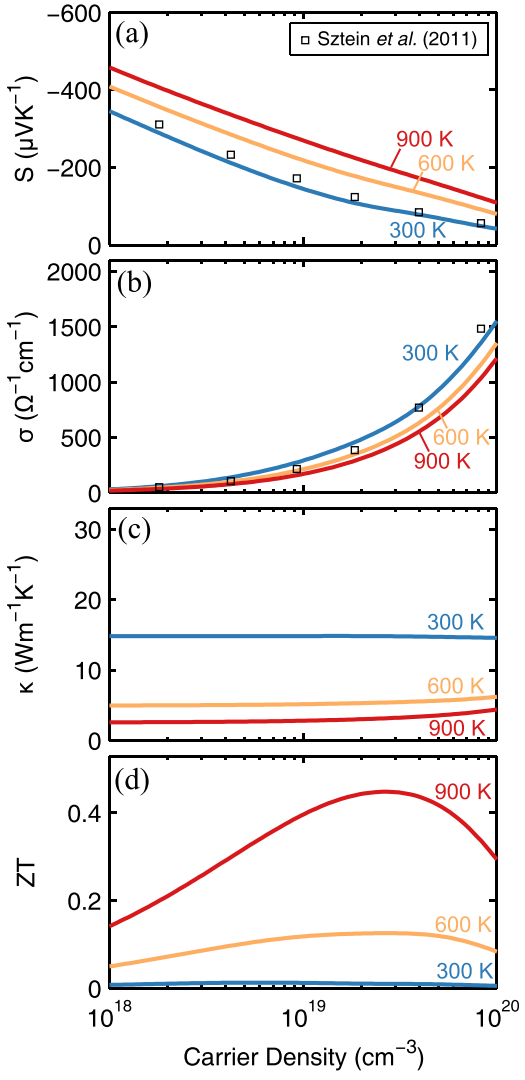

FIG. 2. Modeled (a) Seebeck coefficient, (b) electrical conductivity, (c) thermal conductivity, and (d) ZT at various temperatures versus carrier concentration for $In_{0.1}Ga_{0.9}N$. Square experimental data points are literature measurements for $In_{0.09}Ga_{0.91}N$ at 300 K.[5]

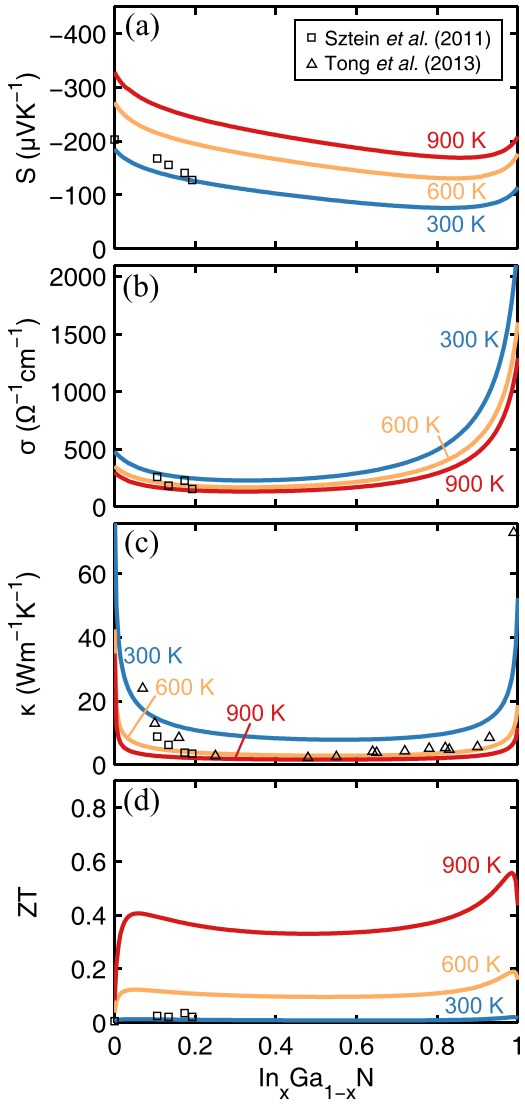

FIG. 3. Modeled (a) Seebeck coefficient, (b) electrical conductivity, (c) thermal conductivity, and (d) ZT at various temperatures versus composition for $In_xGa_{1-x}N$ at carrier density $1 \times 10^{19}\,cm^{-3}$. Square data points represent literature measurements for $In_xGa_{1-x}N$ at 300 K and carrier concentration $1.1 \times 10^{19}\,cm^{-3}$.[5] Triangular data points are measured values for unintentionally doped $In_xGa_{1-x}N$ samples at 300 K.[20]

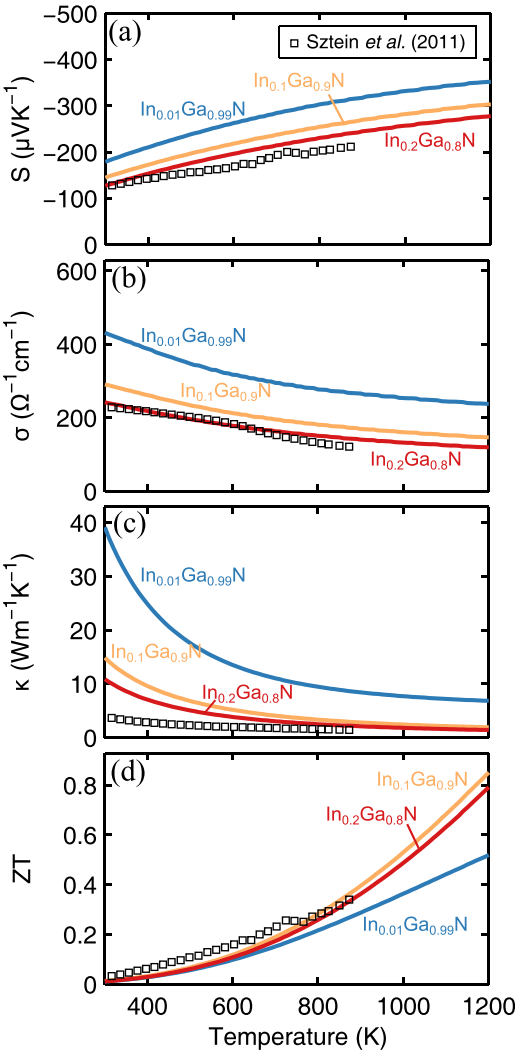

FIG. 4. Modeled (a) Seebeck coefficient, (b) electrical conductivity, (c) thermal conductivity, and (d) ZT for various compositions versus temperature at carrier density $1 \times 10^{19}\,cm^{-3}$. Square data points represent literature data for $In_{0.17}Ga_{0.83}N$ at room temperature carrier density $1.1 \times 10^{19}\,cm^{-3}$.[5]

alloy scattering away from the binary compositions. Figure 1(b) shows the scattering times calculated for phonons versus $\hbar\omega/k_bT$. Under typical experimental conditions for a ternary III-nitride material alloy, mass defect scattering is the dominant scattering mechanism. It is important to keep in mind that the normal scattering term shown here is not a resistive process and thus only indirectly affects thermal conductivity, as described in Sec. III. Mass defect scattering includes the effects of both silicon dopant atoms and alloy elements. While the mass defect scattering lowers thermal conductivity to acceptable thermoelectric values, these same impurity atoms lower electron mobility, thus creating a tradeoff between electrical and thermal properties.

Figure 2 shows the Seebeck coefficient, electrical conductivity, thermal conductivity, and ZT calculated for $In_{0.1}Ga_{0.9}N$ at 300 K, 600 K, and 900 K versus carrier density. Also shown are literature experimental data points for $In_{0.09}Ga_{0.91}N$ at 300 K.[5] The Seebeck coefficient decreases and electrical conductivity increases with increasing carrier concentration while thermal conductivity remains relatively constant. An optimum carrier density at which ZT is maximized exists for each temperature and increases from $1 \times 10^{19}\,cm^{-3}$ at 300 K to $3 \times 10^{19}\,cm^{-3}$ at 900 K. These results are all in excellent agreement with available experimental data, providing an important validation for the calculations presented in this work.

The thermoelectric properties of $In_xGa_{1-x}N$ with a carrier density of $1 \times 10^{19}\,cm^{-3}$ are shown in Figure 3 at 300 K, 600 K, and 900 K. Room temperature literature measurements for $In_xGa_{1-x}N$ at carrier concentration $1.1 \times 10^{19}\,cm^{-3}$ and $In_xGa_{1-x}N$ with unintentional doping (UID) are included for comparison.[5,20] Seebeck coefficient, electrical conductivity, and thermal conductivity are all seen to decrease near the center of the composition range. The electrical and thermal conductivities are reduced due to the additional alloy atoms scattering electrons and phonons at compositions away from the binary endpoints. The Seebeck coefficient is reduced as alloy scattering becomes dominant

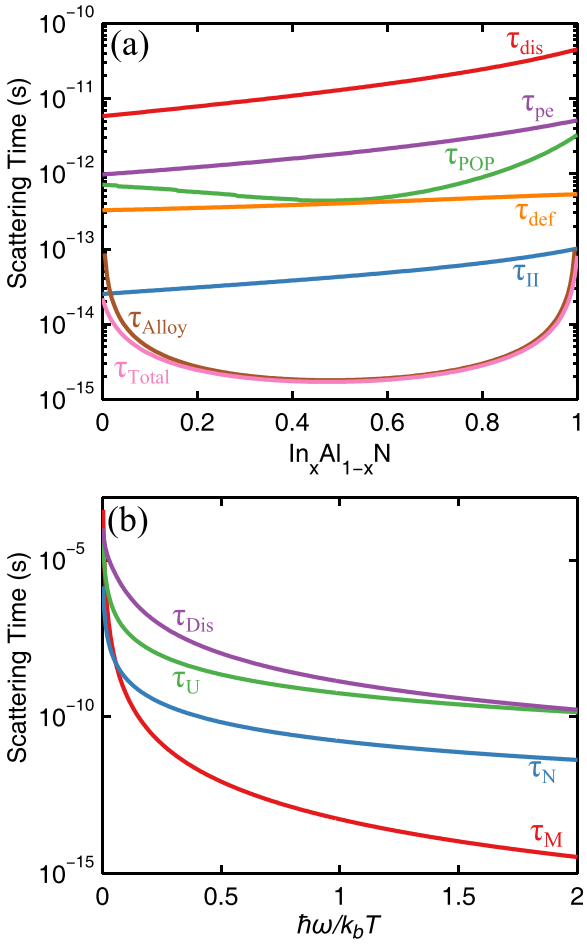

FIG. 5. (a) Electron scattering times versus composition for $In_xAl_{1-x}N$ at 300 K and 4×10^{19} cm^{-3} carrier concentration. (b) Phonon scattering times versus $\hbar\omega/k_bT$ at $In_{0.18}Al_{0.82}N$, 300 K, and 4×10^{19} cm^{-3} carrier concentration.

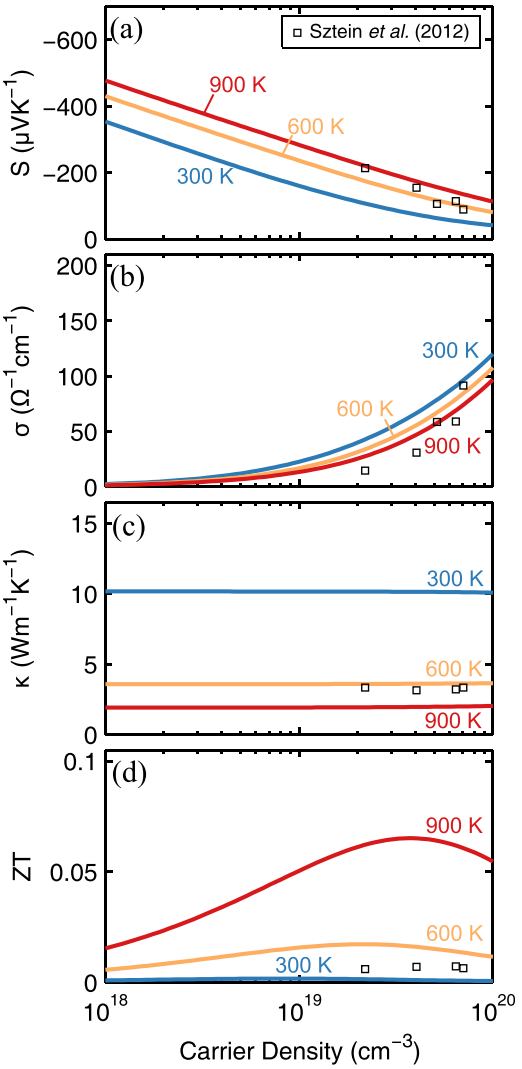

FIG. 6. Modeled (a) Seebeck coefficient, (b) electrical conductivity, (c) thermal conductivity, and (d) ZT at various temperatures versus carrier concentration for $In_{0.18}Al_{0.82}N$ at 300 K. Square experimental data points are for $In_{0.19}Al_{0.81}N$ at room temperature.[13]

due to the less favorable energy dependence of alloy scattering as compared to ionized impurity scattering. It has been shown previously that increased scattering of low energy electrons leads to higher Seebeck coefficients, an effect which is also known as carrier energy filtering.[7] The calculated ZT displays peak values near $In_{0.1}Ga_{0.9}N$ and $In_{0.98}Ga_{0.02}N$. Good agreement with literature values is seen in Figures 3(a) and 3(b).

Although the agreement between calculated and experimental values for InGaN is excellent for electrical properties over a wide range of carrier densities and compositions, calculated room temperature thermal conductivities are higher than experimentally reported values, as can be seen in Figure 3(c). Potential causes for this discrepancy include boundary scattering in experimental thin film samples, the presence of strain and higher than expected defect levels from heteroepitaxy, uncertainty of materials constants such as the Grüneisen parameter, and experimental error. At intermediate indium compositions nanometer-scale compositional inhomogeneities have also been proposed as a potential source of this discrepancy.[20] In order to gauge the potential impact of these factors, additional calculations were performed which include boundary scattering following the work of Holland.[43] The inclusion of this additional scattering mechanism was seen to greatly improve the fit to experimental data. Although better agreement was observed with the inclusion of boundary scattering, this scattering mechanism is not included in the presented results to avoid complications due to sample geometry. Boundary scattering is highly dependent on sample size and an interfacial fitting parameter. Any error caused by the omission of this scattering mechanism would be greatly reduced for the larger sample dimensions typical of thermoelectric devices.

The highest ZT values for $In_xGa_{1-x}N$ are seen for compositions near InN; however, as compositions approach InN, the thermal stability and band gap decrease significantly, calling into question the suitability of these materials at high temperatures. The relative thermal stability of materials can be compared using the difference between their melting points. InN has a melting point of 1373 K, while GaN has a melting point of 2773 K, indicating that compositions near InN will thermally degrade well before compositions near GaN.[1] In addition, the band gap of InN is 0.77 eV which,

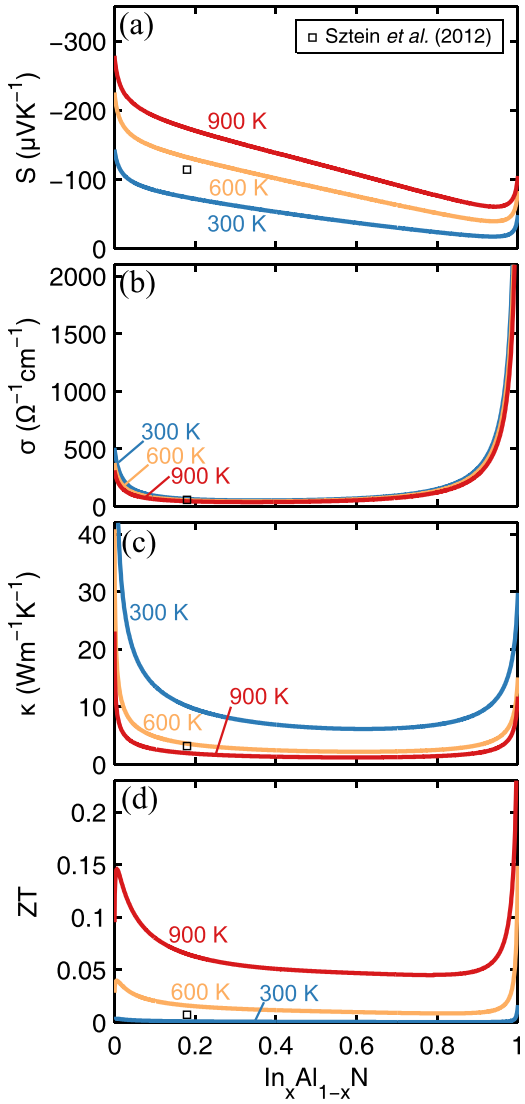

FIG. 7. Modeled (a) Seebeck coefficient, (b) electrical conductivity, (c) thermal conductivity, and (d) ZT at various temperatures versus composition for $In_xAl_{1-x}N$ at carrier density $4 \times 10^{19}\,cm^{-3}$. Square experimental data points are for $In_xAl_{1-x}N$ at room temperature carrier density of $6.4 \times 10^{19}\,cm^{-3}$.[13]

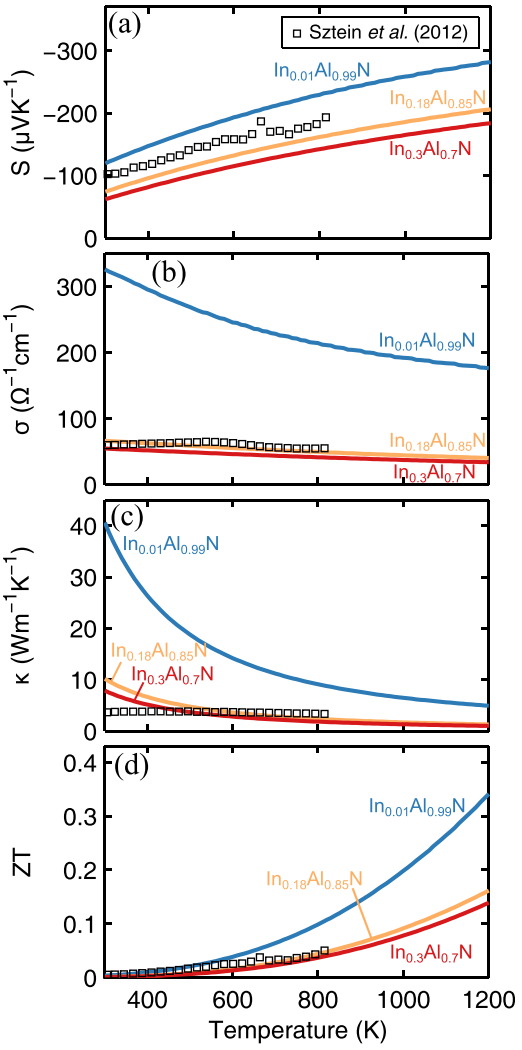

FIG. 8. Modeled (a) Seebeck coefficient, (b) electrical conductivity, (c) thermal conductivity, and (d) ZT for various InAlN compositions versus temperature at carrier density $4 \times 10^{19}\,cm^{-3}$. Square experimental data points are for $In_{0.19}Al_{0.81}N$ at room temperature carrier density of $6.4 \times 10^{19}\,cm^{-3}$.[13]

when using the $\sim 10 k_B T$ minimum band gap rule of thumb as given by Sofo *et al.*, results in a maximum operating temperature of ~900 K which is insufficient for many high temperature applications.[44] This maximum operating temperature is not visible in the current work because the model described above does not take into account thermal excitation of intrinsic carriers across the band gap, resulting in an overestimation of Seebeck coefficient and electrical conductivity at high temperatures when compositions approach InN. This is not a concern for compositions near GaN or AlN since both have significantly larger band gaps of 3.42 eV and 6.2 eV, respectively.[1] Given these limitations intrinsic to indium rich materials, the current work focuses on compositions near GaN and AlN, where thermal stability and band gap remain favorable for high temperature applications. As a point of reference, silicon germanium ($Si_{0.8}Ge_{0.2}$) is a typical high temperature thermoelectric material and has a melting point of ~1550 K, a band gap of ~1 eV, and a maximum ZT of 0.9 near 1200 K.[6,45]

Temperature dependent properties of InGaN at various compositions with carrier density $1 \times 10^{19}\,cm^{-3}$ are displayed in Figure 4. The Seebeck coefficient increases while electrical conductivity and thermal conductivity decrease with increasing temperature. ZT increases with temperature and reaches 0.85 at 1200 K for $In_{0.1}Ga_{0.9}N$. Also shown are experimental data points for $In_{0.17}Ga_{0.83}N$ at a carrier density of $1.1 \times 10^{19}\,cm^{-3}$.[5] Seebeck coefficient and electrical conductivity are seen to match experimental values well while thermal conductivities at low temperatures are higher than experimental values, likely for the same reasons described above. Good thermal conductivity agreement is obtained at moderate to high temperatures as the relative importance of Umklapp scattering increases. The detailed comparison of calculated results with experimental values provides a crucial validation of this model and its ability to predict thermoelectric properties for not only InGaN but also InAlN and AlGaN.

B. InAlN

Figure 5(a) shows electron scattering times for $In_xAl_{1-x}N$. Ionized impurity and alloy scattering are the two

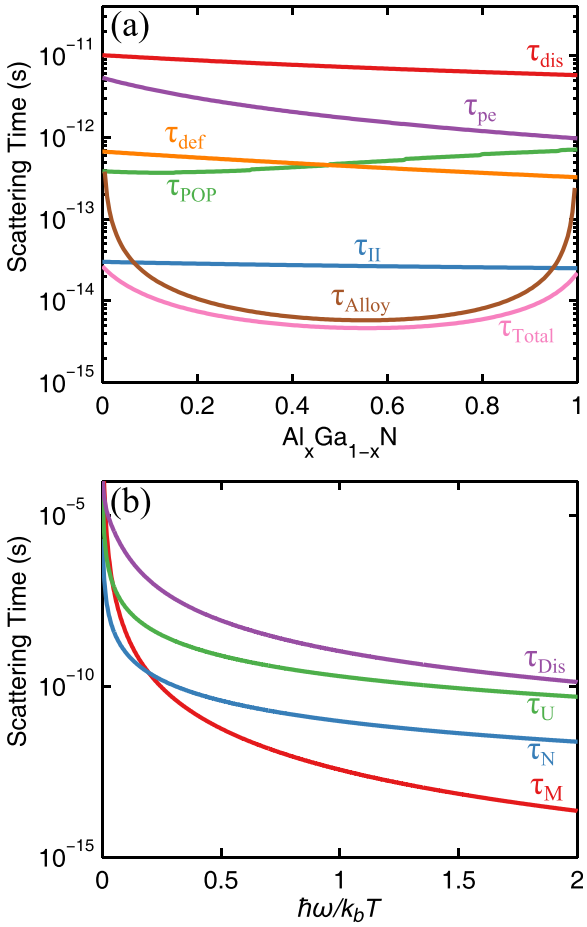

FIG. 9. (a) Electron scattering times versus composition for $Al_xGa_{1-x}N$, 300 K, and $4 \times 10^{19}\,cm^{-3}$ carrier concentration. (b) Phonon scattering times versus $\hbar\omega/k_bT$ for $Al_{0.15}Ga_{0.85}N$, 300 K, and $4 \times 10^{19}\,cm^{-3}$ carrier concentration.

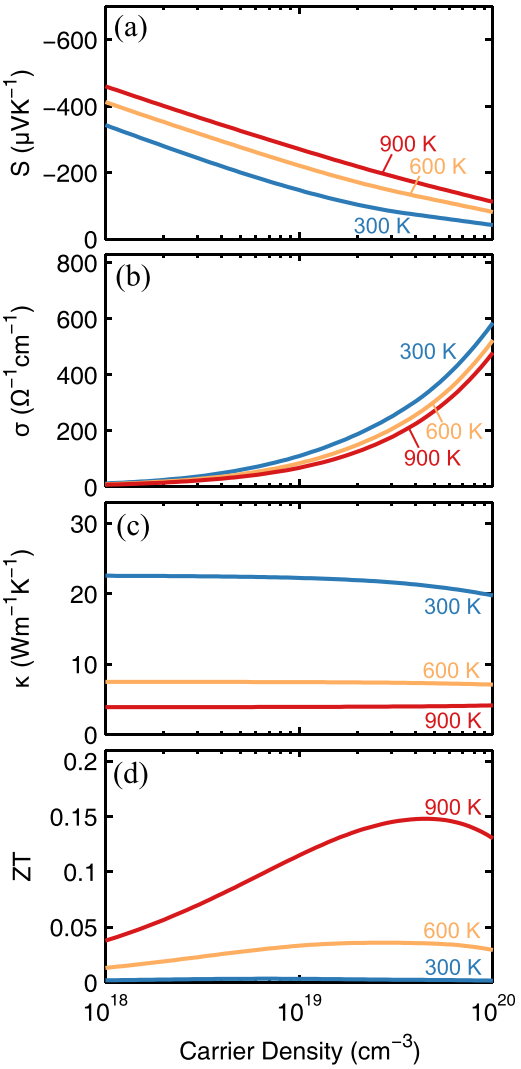

FIG. 10. Modeled (a) Seebeck coefficient, (b) electrical conductivity, (c) thermal conductivity, and (d) ZT at various temperatures versus carrier concentration for $Al_{0.15}Ga_{0.85}N$ at 300 K.

dominant scattering mechanisms for the entire range of compositions and temperatures in this study. It is worth noting here that, despite the large dislocation density, scattering due to dislocations is effectively screened by the high charge densities at which power factors are optimized. Figure 5(b) shows phonon relaxation times, with mass defect scattering as the dominant phonon scattering mechanism.

The Seebeck coefficient, electrical conductivity, thermal conductivity, and ZT are calculated for $In_{0.18}Al_{0.82}N$ versus carrier concentration at 300 K, 600 K, and 900 K and are presented in Figure 6. The optimum carrier density increases with temperature and ranges from $9 \times 10^{18}\,cm^{-3}$ for 300 K to $4 \times 10^{19}\,cm^{-3}$ for 900 K. Some discrepancy is seen between calculated and literature values. This error could be due to experimental error, which is particularly high for InAlN as a result of complicating interfacial effects.[13] The material constants for InAlN are another potential source of error given the small body of literature available on this material. Similar to InGaN, calculated thermal conductivities are higher than those measured on thin film samples. Potential reasons for this include boundary scattering, strain, and higher than expected dislocation densities in experimental samples as well as experimental error and uncertainty in material constants.

Figure 7 shows calculated thermoelectric properties versus composition for $In_xAl_{1-x}N$ at 300 K, 600 K, and 900 K. Carrier concentration is set to $4 \times 10^{19}\,cm^{-3}$. The Seebeck coefficient, electrical conductivity, and thermal conductivity all decrease as the alloy composition moves away from the binary endpoints. Maximum ZT values are very close to both binary endpoints due to alloy scattering rapidly reducing the electrical conductivity.

Temperature dependent properties of $In_{0.01}Al_{0.99}N$, $In_{0.18}Al_{0.82}N$, and $In_{0.3}Al_{0.7}N$ at a carrier density of $4 \times 10^{19}\,cm^{-3}$ are shown in Figure 8. The Seebeck coefficient increases while electrical and thermal conductivities decrease at high temperature for all compositions. ZT increases with temperature and reaches 0.33 at 1200 K for $In_{0.01}Al_{0.99}N$. ZT values for $In_xAl_{1-x}N$ are lower than those seen for $In_xGa_{1-x}N$ due primarily to its very high alloy scattering potential, which results in lower electrical conductivity. The high alloy scattering in this material is not surprising given the vastly different binary constituents of AlN ($E_g = 6.3$ eV) and InN ($E_g = 0.77$ eV).[1] Similar to $In_xGa_{1-x}N$, the agreement between calculated thermal conductivity and literature values is greatly improved at high temperatures as Umklapp scattering gains importance.

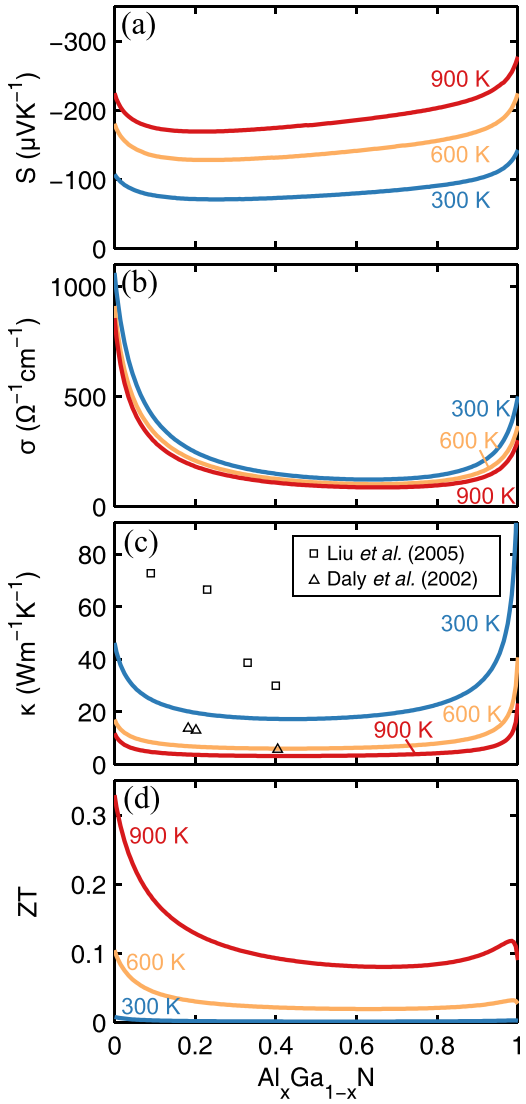

FIG. 11. Modeled (a) Seebeck coefficient, (b) electrical conductivity, (c) thermal conductivity, and (d) ZT for various temperatures versus composition for $Al_xGa_{1-x}N$ at carrier density 4×10^{19} cm^{-3}. Square and triangular data points represent literature measurements for unintentionally doped $Al_xGa_{1-x}N$ at 300 K.[42,46]

The calculated results for $In_{0.18}Al_{0.82}N$ are of particular interest since this composition is lattice matched to GaN, making the growth of thick films on GaN templates possible, which could be of interest for the integration of thermoelectrics with existing GaN based devices. Compositions near InN are less interesting due to the thermal stability and small band gap limitations described above.

C. AlGaN

Scattering times for $Al_xGa_{1-x}N$ are shown in Figure 9(a). Just as for $In_xGa_{1-x}N$ and $In_xAl_{1-x}N$, alloy scattering and ionized impurity scattering are the two dominant scattering mechanisms. Figure 9(b) shows phonon scattering times versus $\hbar\omega/k_bT$ for $Al_{0.15}Ga_{0.85}N$ at 300 K and 4×10^{19} cm^{-3} carrier concentration. Mass defect scattering is found to be the dominant scattering mechanism.

Figure 10 shows the calculated carrier density dependent thermoelectric properties for $Al_{0.15}Ga_{0.85}N$ at 300 K, 600 K, and 900 K. The Seebeck coefficient decreases with increasing carrier concentration while electrical conductivity increases and thermal conductivity remains relatively constant. Optimum carrier density varies from 7×10^{18} cm^{-3} at 300 K to 4×10^{19} cm^{-3} at 900 K.

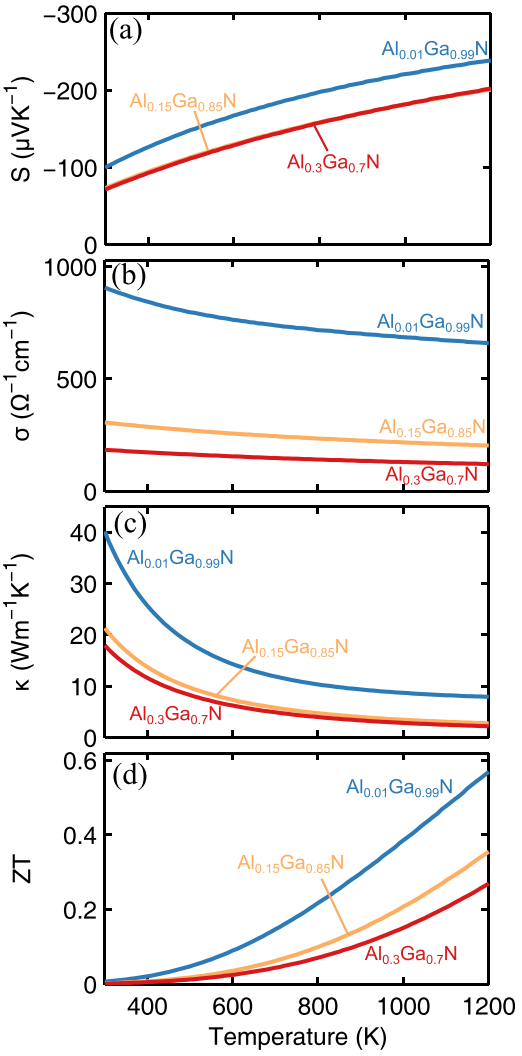

FIG. 12. Modeled (a) Seebeck coefficient, (b) electrical conductivity, (c) thermal conductivity, and (d) ZT at various compositions versus temperature for $Al_{0.15}Ga_{0.85}N$ at carrier density 4×10^{19} cm^{-3}.

The Seebeck coefficient, electrical conductivity, thermal conductivity, and ZT for $Al_xGa_{1-x}N$ at 300 K, 600 K, and 900 K and a room temperature carrier density 4×10^{19} cm^{-3} are plotted in Figure 11. Although it can be seen that the calculated thermal conductivities fall within the range of available experimental values, a meaningful comparison is difficult due to the large spread in measured thermal conductivities, which is likely caused by significant variations in impurities, dislocations, and differing measurement techniques.[42,46] The Seebeck coefficient, electrical conductivity, and thermal conductivity are all seen to be highest at the two binary alloys. The interplay of these trends results in two maximum ZT values at 0% AlN and at approximately $Al_{0.97}Ga_{0.03}N$.

Figure 12 shows the temperature dependent properties of various AlGaN compositions at a room temperature carrier density of 4×10^{19} cm^{-3}. The Seebeck coefficient

increases while electrical and thermal conductivities decrease with increasing temperature. ZT increases with temperature for all compositions and reaches 0.57 for $Al_{0.01}Ga_{0.99}N$ at 1200 K.

The thermoelectric properties of $Al_xGa_{1-x}N$ are not as promising as those of $In_xGa_{1-x}N$ due to both higher thermal conductivity and lower electrical conductivity. The lower thermal conductivities seen in $In_xGa_{1-x}N$ and $In_xAl_{1-x}N$ are driven primarily by the large indium atoms since phonon mass defect scattering is a function of both atomic weight squared and atomic radius squared, as can be seen in Eqs. (30) and (31). The relatively small aluminum atoms provide less mass defect scattering and thus less reduction of thermal conductivity than the larger indium atoms. Additionally, the $Al_xGa_{1-x}N$ material system does not provide a corresponding improvement in electrical properties due to its high alloy scattering potential, resulting in lower ZT values than calculated $In_xGa_{1-x}N$.

V. CONCLUSIONS

Thermoelectric properties for n-type III-nitride alloys are calculated in the current work using the Boltzmann transport equation with the relaxation time approximation for electron transport and the Callaway model for phonon transport. The accuracy of calculated values is confirmed through comparison to experimental data. Ionized impurity and alloy scattering are identified as the dominant electron scattering mechanisms across the range of carrier densities, compositions, and temperatures relevant for thermoelectric applications. Mass defect scattering is similarly identified as the dominant scattering mechanism for phonons at conditions appropriate for thermoelectric applications. $In_xGa_{1-x}N$ shows the most promising ZT values reaching 0.85 at 1200 K, which approaches the commercially favored n-type SiGe ZT of ~0.9 at a similar temperature.[6] $Al_xGa_{1-x}N$ and $In_xAl_{1-x}N$ have lower ZT values due to their high lattice thermal conductivity and low electron mobilities.

ACKNOWLEDGMENTS

The authors would like to thank the UCSB thermoelectrics group, particularly Professor Gossard, Ben Curtin, and Peter Burke for helpful discussions. This work was supported as part of the Center for Energy Efficient Materials, an Energy Frontier Research Center funded by the U.S. Department of Energy, Office of Science, Basic Energy Sciences under Award Number DE-SC0001009.

[1]H. Morkoc, *Handbook of Nitride Semiconductors and Devices* (Wiley-VHC, Weinheim, 2008), Vols. I-III.
[2]E. Matioli, C. Neufeld, M. Iza, S. C. Cruz, A. A. Al-Heji, X. Chen, R. M. Farrell, S. Keller, S. DenBaars, U. Mishra, S. Nakamura, J. Speck, and C. Weisbuch, Appl. Phys. Lett. **98**, 021102 (2011).
[3]B. N. Pantha, R. Dahal, J. Li, J. Y. Lin, H. X. Jiang, and G. Pomrenke, Appl. Phys. Lett. **92**, 042112 (2008).
[4]W. L. Liu and A. A. Balandin, J. Appl. Phys. **97**, 123705 (2005).
[5]A. Sztein, H. Ohta, J. E. Bowers, S. P. DenBaars, and S. Nakamura, J. Appl. Phys. **110**, 123709 (2011).
[6]T. M. Tritt and M. A. Subramanian, MRS Bull. **31**, 188 (2006).
[7]A. Shakouri and M. Zebarjadi, in *Thermal Nanosystems and Nanomaterials* (Springer-Verlag, Berlin, 2009), pp. 225–299.
[8]S. A. Jewett, M. S. Makowski, B. Andrews, M. J. Manfra, and A. Ivanisevic, Acta Biomater. **8**, 728 (2012).
[9]S. Yamaguchi, R. Izaki, N. Kaiwa, and A. Yamamoto, Appl. Phys. Lett. **86**, 252102 (2005).
[10]N. Kaiwa, M. Hoshino, T. Yaginuma, R. Izaki, S. Yamaguchi, and A. Yamamoto, Thin Solid Films **515**, 4501 (2007).
[11]B. N. Pantha, R. Dahal, J. Li, J. Y. Lin, H. X. Jiang, and G. Pomrenke, J. Electron. Mater. **38**, 1132 (2009).
[12]E. N. Hurwitz, M. Asghar, A. Melton, B. Kucukgok, L. Su, M. Orocz, M. Jamil, N. Lu, and I. T. Ferguson, J. Electron. Mater. **40**, 513 (2011).
[13]A. Sztein, J. E. Bowers, S. P. DenBaars, and S. Nakamura, J. Appl. Phys. **112**, 083716 (2012).
[14]H. Tong, J. Zhang, G. Liu, J. A. Herbsommer, G. S. Huang, and N. Tansu, Appl. Phys. Lett. **97**, 112105 (2010).
[15]J. Zhang, H. Tong, G. Liu, J. A. Herbsommer, G. S. Huang, and N. Tansu, J. Appl. Phys. **109**, 053706 (2011).
[16]B. N. Pantha, I. Feng, K. Aryal, J. Li, J. Lin, and H. X. Jiang, Appl. Phys. Express **4**, 051001 (2011).
[17]S. Yamaguchi, Y. Iwamura, and A. Yamamoto, Appl. Phys. Lett. **82**, 2065 (2003).
[18]A. Sztein, H. Ohta, J. Sonoda, A. Ramu, J. E. Bowers, S. P. DenBaars, and S. Nakamura, Appl. Phys. Express **2**, 111003 (2009).
[19]H. Tong, H. Zhao, V. A. Handara, J. A. Herbsommer, and N. Tansu, in *Proceedings of the International Society for Optical Engineering* (2009), p. 721103.
[20]T. Tong, D. Fu, A. X. Levander, W. J. Schaff, B. N. Pantha, N. Lu, B. Liu, I. Ferguson, R. Zhang, J. Y. Lin, H. X. Jiang, J. Wu, and D. G. Cahill, Appl. Phys. Lett. **102**, 121906 (2013).
[21]J. H. Bahk, Ph.D. dissertation, University of California, Santa Barbara, CA, 2010.
[22]M. Lundstrom, *Fundamentals of Carrier Transport* (Cambridge University Press, 2000).
[23]C. Bera, M. Soulier, C. Navone, G. Roux, J. Simon, S. Volz, and N. Mingo, J. Appl. Phys. **108**, 124306 (2010).
[24]C. Vineis, T. Harman, S. Calawa, M. Walsh, R. Reeder, R. Singh, and A. Shakouri, Phys. Rev. B **77**, 235202 (2008).
[25]A. E. Wickenden, L. B. Rowland, K. Doverspike, D. K. Gaskill, J. A. Freitas, D. S. Simons, and P. H. Chi, J. Electron. Mater. **24**, 1547 (1995).
[26]D. Kotchetkov, J. Zou, A. A. Balandin, D. I. Florescu, and F. H. Pollak, Appl. Phys. Lett. **79**, 4316 (2001).
[27]J. Simon, A. Wang, H. Xing, S. Rajan, and D. Jena, Appl. Phys. Lett. **88**, 042109 (2006).
[28]M. Farahmand, C. Garetto, E. Bellotti, K. F. Brennan, M. Goano, E. Ghillino, G. Ghione, J. D. Albrecht, and P. P. Ruden, IEEE Trans. Electron Devices **48**, 535 (2001).
[29]B. E. Foutz, S. K. O'Leary, M. S. Shur, and L. F. Eastman, J. Appl. Phys. **85**, 7727 (1999).
[30]A. T. Ramu, L. E. Cassels, N. H. Hackman, H. Lu, J. M. O. Zide, and J. E. Bowers, J. Appl. Phys. **107**, 083707 (2010).
[31]M. Vaughan and B. Ridley, Phys. Rev. B **72**, 075211 (2005).
[32]J. W. Harrison and J. R. Hauser, Phys. Rev. B **13**, 5347 (1976).
[33]M. A. Littlejohn, J. R. Hauser, T. H. Glisson, D. K. Ferry, and J. W. Harrison, Solid-State Electronics. **21**, 107 (1978).
[34]V. W. L. Chin, B. Zhou, T. L. Tansley, and X. Li, J. Appl. Phys. **77**, 6064 (1995).
[35]B. K. Ridley, B. E. Foutz, and L. F. Eastman, Phys. Rev. B **61**, 16862 (2000).
[36]D. C. Look and J. R. Sizelove, Phys. Rev. Lett. **82**, 1237 (1999).
[37]J. Zou, D. Kotchetkov, A. A. Balandin, D. I. Florescu, and F. H. Pollak, J. Appl. Phys. **92**, 2534 (2002).
[38]J. Callaway, Phys. Rev. **113**, 1046 (1959).
[39]B. Abeles, Phys. Rev. **131**, 1906 (1963).
[40]M. Asen-Palmer, K. Bartkowski, E. Gmelin, M. Cardona, A. Zhernov, A. Inyushkin, A. Taldenkov, V. Ozhogin, K. Itoh, and E. Haller, Phys. Rev. B **56**, 9431 (1997).
[41]D. Morelli, J. Heremans, and G. Slack, Phys. Rev. B **66**, 195304 (2002).
[42]W. L. Liu and A. A. Balandin, J. Appl. Phys. **97**, 073710 (2005).
[43]M. G. Holland, Phys. Rev. **132**, 2461 (1963).
[44]J. Sofo and G. Mahan, Phys. Rev. B **49**, 4565 (1994).
[45]G. L. McVay and A. R. DuCharme, Phys. Rev. B **9**, 627 (1974).
[46]B. C. Daly, H. J. Maris, A. V. Nurmikko, M. Kuball, and J. Han, J. Appl. Phys. **92**, 3820 (2002).
[47]A. AlShaikhi and G. P. Srivastava, J. Appl. Phys. **103**, 083554 (2008).
[48]D. Jena, S. Heikman, J. Speck, A. Gossard, U. Mishra, A. Link, and O. Ambacher, Phys. Rev. B **67**, 153306 (2003).